

Solution landscape of a reduced Landau–de Gennes model on a hexagon

Yucen Han¹, Jianyuan Yin², Pingwen Zhang², Apala Majumdar³, and Lei Zhang⁴

¹*Beijing International Center for Mathematical Research, Peking University, Beijing 100871, China.*

²*School of Mathematical Sciences, Laboratory of Mathematics and Applied Mathematics, Peking University, Beijing 100871, China.*

³*Department of Mathematics and Statistics, University of Strathclyde, Glasgow, G1 1XH, United Kingdom.*

⁴*Beijing International Center for Mathematical Research, Center for Quantitative Biology, Peking University, Beijing 100871, China.*

We investigate the solution landscape of a reduced Landau–de Gennes model for nematic liquid crystals on a two-dimensional hexagon at a fixed temperature, as a function of λ —the edge length. This is a generic example for reduced approaches on regular polygons. We apply the high-index optimization-based shrinking dimer method to systematically construct the solution landscape consisting of multiple defect solutions and relationships between them. We report a new stable T state with index-0 that has an interior $-1/2$ defect; new classes of high-index saddle points with multiple interior defects referred to as H class and TD class; changes in the Morse index of saddle points with λ^2 and novel pathways mediated by high-index saddle points that can control and steer dynamical pathways. The range of topological degrees, locations and multiplicity of defects offered by these saddle points can be used to navigate through complex solution landscapes of nematic liquid crystals and other related soft matter systems.

I. INTRODUCTION

Nematic liquid crystals (NLCs) are viscoelastic anisotropic materials that combine the fluidity of liquids with the orientational order of solids. The electro-optic properties of NLCs make them the working materials of choice for the multi-billion dollar liquid crystal display (LCD) industry. NLCs have tremendous potential in nanoscience, biophysics and material design, all of which rely on modeling and computational methods for studying stable/unstable NLC states, switching mechanisms, dynamical processes on energy landscapes etc. [1]. These approaches are useful for soft matter systems in general, for the study of interfacial phenomena, active matter, polymers, etc. [2–5]. A particularly intriguing feature of NLCs is topological defects, which are discontinuities in nematic directors or the averaged special directions of orientational ordering. Defects commonly exist as isolated points or disclination lines in experiments [6]. Defects play important roles in physical phenomena, e.g. multistability in confinement, switching processes, self-assembly processes, materials design with defects as binding sites and colloid science [7, 8].

NLCs in confinement typically have multiple stable states that are stationary points of an appropriately defined free energy. The energy landscape of the NLC system is determined by the material properties, temperature, size and shape of the domain, boundary effects and external fields. In particular, the Landau–de Gennes (LdG) theory has been extensively applied in recent years to investigate the energy landscape of NLCs in confinement [7, 9–11], and there has been substantial analytic progress for the study of energy minima in confinement [12–15].

The confined NLC system can switch between different stable states by means of an external field, thermal fluctuations, noise and mechanical perturbations. The switching requires the system to cross an energy barrier through a transition state. The transition state is an index-1 saddle point, i.e., a stationary point where the corresponding Hessian of the free energy has one and only one negative eigenvalue [16]. The transition state has the highest energy along the transition pathway that connects two neighbouring stable states. The reader is referred to [17] for transition pathways on a square domain with tangent boundary conditions and to [18] for transition pathways on a cylindrical domain with homeotropic boundary conditions.

There is substantial recent interest in high-index saddle points of the LdG free energy, which are stationary points of the free energy, and the Morse index is the number of negative eigenvalues of the corresponding Hessian of the free energy [19]. For example, minimizing stationary points have index 0 and transition states are index-1 saddle points. In recent years, powerful numerical algorithms have been developed to find multiple solutions of nonlinear equations, including the minimax method [20], the deflation technique [21], the eigenvector-following method [22], and the homotopy method [23, 24]. Despite substantial progress in this direction, the relationships between different solutions are unclear. In a recent work [25], Yin *et al.* propose a general numerical method that constructs the pathway map of NLCs confined on a square domain. A hierarchy of connected solutions, including high-index saddle points, is identified on a square domain with tangent boundary conditions. For small nano-scale square domains, it is known that the well order reconstruction solution (WORS) is the unique solution with isotropic diagonals and is the global energy minimum in this asymptotic regime [26, 27]. As the size of the square domain increases, WORS loses stability and its Morse index increases. Using WORS as the parent state (the highest-index saddle) and the high-index optimization-based shrinking dimer (HiOSD) method [28], the authors construct a solution landscape on

the square domain [25] and report novel saddle point solutions with multiple interior defects that were previously unreported in the literature. This construction also offers multiple transition pathways (determined by the choice of the connecting saddle points) connecting the stable diagonal and rotated solutions for large square domains.

In this paper, we apply a reduced LdG model to numerically compute the complex solution landscapes of NLCs confined on a regular two-dimensional (2D) hexagonal domain with tangent boundary conditions. The reduced LdG model is suitable for 2D domains [29] and effectively reduces to the Ginzburg–Landau model for superconductors at a fixed temperature, which is representative of temperatures below the NLC supercooling temperature [30]. In this reduced approach, we only have two parameters—the topological degree of the tangent boundary conditions and the domain size λ^2 . We largely vary λ and exploit the topological degree to some extent, to construct a hierarchy of stationary points of the reduced LdG free energy on the hexagonal domain. The hierarchy includes the previously reported Ring, Para (P) and Meta (M) solutions in [31], which are distinguished by the locations, degrees and multiplicities of their defects. Furthermore, we find entirely new classes of high-index saddle points, e.g. the TD class (including index-6 saddle points) and the H class (including an index-14 saddle point). The parent state on a hexagon changes from the Ring solution, to the T135 saddle point, and to the index-14 H-type saddle point as λ increases. It is noteworthy that we find a new type of index-0 stable solution with an interior $-1/2$ defect, referred to as the T solution with a stable interior $-1/2$ defect. We also observe certain numerical trends on how the vertex profile (bend-like versus splay-like) affects the Morse index as does the symmetry group of the saddle point. A plethora of saddle point solutions gives us diverse possibilities for transition pathways and indeed, we illustrate the differences between transition pathways with transition states (index-1 saddle points) and transition pathways with high-index saddle points, e.g. two stable T solutions can be connected by an index-8 H-type saddle point. Some pairs of stable solutions are incompatible with transition states; they cannot be connected by a single transition state, e.g. two stable T solutions or indeed two different solutions in the P class, and this can be used to either impede or enhance switching for tailor-made applications.

There are deep analytic issues associated with saddle points of nonlinear and non-convex functionals, such as the reduced LdG free energy. We speculate that the saddle points of the reduced LdG model can be interpreted as minimizers of constrained problems or appropriately defined Dirichlet problems, as the WORS in [27]. Advances in this direction would lead to new control strategies for confined NLC systems, since we could propose conditions that would stabilise the saddle point solutions, some of which have multiple interior and boundary defects. Secondly, the hexagon is a generic regular polygon with an even number of sides. Our numerical results, at least from qualitative aspects, will carry over to arbitrary regular polygons with an even number of sides, and indeed to a large number of phase field models on 2D polygons with planar boundary conditions. Our results are indeed a consequence of the symmetry of the domain and the mathematical formulation, and as such, reveal certain universal trends of complex solution landscapes with regards to geometry, confinement and defects.

In Section II, we briefly review the reduced LdG framework for NLCs on 2D domains. In Section III, we review the HiOSD method for computing index- k saddle points to construct the solution landscape. In Section IV, we systematically construct the solution landscapes with increasing complexity for $\lambda^2 = 70, 120$ and 600 respectively, where the parameter λ^2 is a measure of the hexagonal domain size. In Section V, we compare the solution landscapes on square and hexagonal domains and we present our conclusions and perspectives in Section VI.

II. LANDAU–DE GENNES THEORY

As a powerful continuum theory for NLCs, the LdG theory describes the NLC state with a macroscopic order parameter—the \mathbf{Q} -tensor, which is a symmetric, traceless 3×3 matrix [1]. The NLC is said to be in the isotropic phase if $\mathbf{Q} = 0$, uniaxial if \mathbf{Q} has a pair of degenerate nonzero eigenvalues, and biaxial if \mathbf{Q} has three distinct eigenvalues. A uniaxial \mathbf{Q} -tensor is often written compactly as

$$\mathbf{Q} = s \left(\mathbf{n} \otimes \mathbf{n} - \frac{\mathbf{I}}{3} \right), \quad (1)$$

where \mathbf{n} is the nematic director (i.e., the eigenvector with the non-degenerate eigenvalue) that models the single preferred direction of orientational ordering and \mathbf{I} is the identity matrix.

We work with a particularly simple form of the LdG energy

$$I[\mathbf{Q}] := \int_{\Omega_\lambda} \left[\frac{L}{2} |\nabla \mathbf{Q}|^2 + f_b(\mathbf{Q}) \right] dA, \quad (2)$$

where Ω_λ is a 2D hexagonal domain with the edge length λ , $|\nabla \mathbf{Q}|^2 = \frac{\partial Q_{ij}}{\partial r_k} \frac{\partial Q_{ij}}{\partial r_k}$ is the elastic potential, and f_b is the

bulk potential that drives the isotropic-nematic phase transition as a function of the temperature,

$$f_b = \frac{A}{2} \text{tr} \mathbf{Q}^2 - \frac{B}{3} \text{tr} \mathbf{Q}^3 + \frac{C}{4} (\text{tr} \mathbf{Q}^2)^2, \quad (3)$$

where B, C are positive material-dependent constants, and $A = \alpha(T - T^*)$ is the rescaled temperature. For $A < 0$, f_b favours an ordered bulk uniaxial phase and $\mathcal{N} := \{\mathbf{Q} \in \mathbb{M}^{3 \times 3} : \mathbf{Q} = s_+(\mathbf{n} \otimes \mathbf{n} - \mathbf{I}/3)\}$ is the set of minimizers of f_b with

$$s = s_+ := \frac{B + \sqrt{B^2 + 24|A|C}}{4C} \quad (4)$$

and $\mathbf{n} \in \mathbb{S}^2$. We use MBBA as a representative NLC material and use fixed values $B = 0.64 \times 10^4 N/m^2$ and $C = 0.35 \times 10^4 N/m^2$, which are reported in [32].

We nondimensionalize the system with $\bar{r} = r/\lambda$, and the rescaled LdG energy functional is

$$\bar{I}[\bar{\mathbf{Q}}] := \int_{\Omega} \left[\frac{1}{2} |\bar{\nabla} \bar{\mathbf{Q}}|^2 + \frac{\lambda^2}{L} f_b(\bar{\mathbf{Q}}) \right] d\bar{A}, \quad (5)$$

where Ω is a regular polygon with the unit edge length. In what follows, we drop the bars and all statements are in terms of the rescaled variables. The corresponding Euler-Lagrange equations are:

$$\Delta \mathbf{Q} = \frac{\lambda^2}{L} \left(A \mathbf{Q} - B \left(\mathbf{Q} \mathbf{Q} - \frac{|\mathbf{Q}|^2}{3} \mathbf{I} \right) + C |\mathbf{Q}|^2 \mathbf{Q} \right). \quad (6)$$

The physically relevant states are modelled as local or global energy minima subject to the imposed boundary conditions.

In [29], the authors prove that the physically relevant \mathbf{Q} -tensors on 2D domains have a fixed eigenvector \mathbf{z} , the unit vector in the z -direction, and can be written in terms of three variables q_1, q_2, q_3 as shown below:

$$\mathbf{Q} = q_1 (\mathbf{n} \otimes \mathbf{n} - \mathbf{m} \otimes \mathbf{m}) + q_2 (\mathbf{n} \otimes \mathbf{m} + \mathbf{m} \otimes \mathbf{n}) + q_3 (2\mathbf{z} \otimes \mathbf{z} - \mathbf{n} \otimes \mathbf{n} - \mathbf{m} \otimes \mathbf{m}) \quad (7)$$

where \mathbf{n} and \mathbf{m} are orthonormal vectors in the xy -plane [29]. In other words, only three degrees of freedom out of five remain in a 2D framework. Further, in [33], the authors show that for $A = -\frac{B^2}{3C}$, q_3 is a constant for all physically relevant solutions of (6) of the form (7), subject to Dirichlet uniaxial tangent boundary conditions on the domain edges. Hence, for $A = -\frac{B^2}{3C}$, we have a reduced description in terms of a reduced LdG tensor, \mathbf{P} , with only two degrees of freedom such that

$$\mathbf{Q} = \left(\begin{array}{c|c} \mathbf{P}(\mathbf{r}) + \frac{B}{6C} \mathbf{I}_2 & \begin{matrix} 0 \\ 0 \end{matrix} \\ \hline 0 & -B/3C \end{array} \right), \quad (8)$$

where \mathbf{I}_2 is 2×2 identity matrix. In what follows, we track defects by using the nodal set or the zero set of \mathbf{P} that is the set of uniaxial \mathbf{Q} -tensors with the negative order parameter about \mathbf{z} , as can be seen above, which is consistent with disorder in the plane of Ω .

The corresponding reduced LdG energy is

$$E[\mathbf{P}] := \int_{\Omega} \left[\frac{1}{2} |\nabla \mathbf{P}|^2 + \frac{\lambda^2}{L} \left(-\frac{B^2}{4C} \text{tr} \mathbf{P}^2 + \frac{C}{4} (\text{tr} \mathbf{P}^2)^2 \right) \right] dA. \quad (9)$$

The Euler-Lagrange equations for \mathbf{P} of (9) are

$$\begin{cases} \Delta P_{11} = \frac{2C\lambda^2}{L} \left(P_{11}^2 + P_{12}^2 - \frac{B^2}{4C^2} \right) P_{11}, \\ \Delta P_{12} = \frac{2C\lambda^2}{L} \left(P_{11}^2 + P_{12}^2 - \frac{B^2}{4C^2} \right) P_{12}. \end{cases} \quad (10)$$

We further define a parameter

$$\bar{\lambda}^2 = \frac{2C\lambda^2}{L}. \quad (11)$$

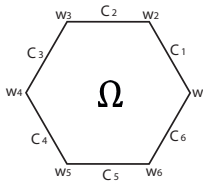


FIG. 1: hexagonal domain

We treat C, L to be fixed material-dependent constants, and therefore $\bar{\lambda}^2$ is proportional to λ^2 . For brevity, we drop the bar over λ and use λ^2 to represent $\frac{2C\lambda^2}{L}$, as a measure of the domain size.

Such reduced descriptions have been hugely successful for 2D systems or thin three-dimensional (3D) systems, both for capturing the qualitative properties of physically relevant solutions and for probing into defect cores [34–38]. In a fully 3D system, there may be other classes of physically relevant solutions, such as escaped solutions, with additional degrees of freedom [18, 33] and this will be pursued in further work.

As illustrated in Figure 1, the regular hexagonal domain Ω is centered at the origin with vertices

$$w_k = \left(\cos \frac{(k-1)\pi}{3}, \sin \frac{(k-1)\pi}{3} \right), \quad k = 1, \dots, 6.$$

Starting from $(1, 0)$, the edges are labeled counterclockwise as C_1, \dots, C_6 , and the distance between a point on $\partial\Omega$ and the vertices is defined as

$$\text{dist}(w) = \min \{ \|w - w_k\|_2, k = 1, \dots, 6 \}, \quad w \in \partial\Omega.$$

The Dirichlet boundary conditions $\mathbf{P} = \mathbf{P}^b$ are imposed on the segments of edges as, away from the vertices

$$\begin{aligned} P_{11}^b(w) &= \alpha_k = -\frac{B}{2C} \cos \left(\frac{(2k-1)\pi}{3} \right), \\ P_{12}^b(w) &= \beta_k = -\frac{B}{2C} \sin \left(\frac{(2k-1)\pi}{3} \right), \end{aligned} \quad w \in C_k, \text{dist}(w) > \epsilon, \quad (12)$$

where $0 < \epsilon \ll 1/2$ is the size of the mismatch region. We point out that the corresponding \mathbf{Q}^b (associated with \mathbf{P}^b in (8)) is in \mathcal{N} . The value at the corner is the average of the two boundary conditions on the two intersecting edges.

The \mathbf{P} -tensor can also be expressed in terms of a scalar order parameter s and an angle γ as

$$\mathbf{P} = s \begin{pmatrix} \cos 2\gamma & \sin 2\gamma \\ \sin 2\gamma & -\cos 2\gamma \end{pmatrix} = 2s \left(\mathbf{n} \otimes \mathbf{n} - \frac{1}{2} \mathbf{I}_2 \right), \quad (13)$$

where $\mathbf{n} = (\cos \gamma, \sin \gamma)^\top$ is the nematic director in the plane, s is a scalar order parameter that measures the degree of planar order about \mathbf{n} . The Dirichlet conditions (12) ensure that \mathbf{n} is tangent to the edges, i.e., either parallel or antiparallel to the edges, so that this is a model 2D problem with tangent or planar boundary conditions. In particular, one can use this representation to define the topological degree of \mathbf{P}^b above, i.e., γ changes by $2\pi k$ radians or \mathbf{n} rotates by $2\pi k$ radians around $\partial\Omega$ for an integer or half integer k and the corresponding topological degree of \mathbf{P}^b is k .

III. NUMERICAL METHOD

A. HiOSD method

As mentioned in the Introduction, it is a numerical challenge to find saddle point solutions, especially those with high indices, of nonlinear systems of partial differential equations such as the Euler-Lagrange equation in Eq. (10). In what follows, we employ the HiOSD method to efficiently compute the stationary points of any index (including minima) for the reduced LdG energy on a hexagon (9) [28]. For a non-degenerate index- k saddle point $\hat{\mathbf{x}}$, the Hessian $\mathbb{H}(\mathbf{x}) = \nabla^2 E(\mathbf{x})$ at $\hat{\mathbf{x}}$ has exactly k negative eigenvalues $\hat{\lambda}_1 \leq \dots \leq \hat{\lambda}_k$ with corresponding unit eigenvectors

$\hat{\mathbf{v}}_1, \dots, \hat{\mathbf{v}}_k$ satisfying $\langle \hat{\mathbf{v}}_j, \hat{\mathbf{v}}_i \rangle = \delta_{ij}$, $1 \leq i, j \leq k$. Define a k -dimensional subspace $\hat{\mathcal{V}} = \text{span}\{\hat{\mathbf{v}}_1, \dots, \hat{\mathbf{v}}_k\}$, then $\hat{\mathbf{x}}$ is a local maximum on a k -dimensional linear manifold $\hat{\mathbf{x}} + \hat{\mathcal{V}}$ and a local minimum on $\hat{\mathbf{x}} + \hat{\mathcal{V}}^\perp$, where $\hat{\mathcal{V}}^\perp$ is the orthogonal complement space of $\hat{\mathcal{V}}$.

The HiOSD dynamics for a k -saddle (k -HiOSD) is given as follows:

$$\begin{cases} \beta^{-1} \dot{\mathbf{x}} = - \left(\mathbf{I} - 2 \sum_{j=1}^k \mathbf{v}_j \mathbf{v}_j^\top \right) \nabla E(\mathbf{x}), \\ \gamma^{-1} \dot{\hat{\mathbf{v}}}_i = - \left(\mathbf{I} - \mathbf{v}_i \mathbf{v}_i^\top - 2 \sum_{j=1}^{i-1} \mathbf{v}_j \mathbf{v}_j^\top \right) \mathbb{H}(\mathbf{x}) \mathbf{v}_i, \quad i = 1, \dots, k, \end{cases} \quad (14)$$

where the state variable \mathbf{x} and k direction variables \mathbf{v}_i are coupled, \mathbf{I} is the identity operator and $\beta, \gamma > 0$ are relaxation parameters. The k -HiOSD dynamics (14) is coupled with an initial condition:

$$\mathbf{x}(0) = \mathbf{x}^0 \in \mathbb{R}^n, \quad \mathbf{v}_i(0) = \mathbf{v}_i^0 \in \mathbb{R}^n, \quad i = 1, \dots, k, \quad (15)$$

where $\mathbf{v}_1^0, \dots, \mathbf{v}_k^0$ satisfy the orthonormal condition $\langle \mathbf{v}_i^0, \mathbf{v}_j^0 \rangle = \delta_{ij}$, $i, j = 1, 2, \dots, k$. The first equation in (14) describes a transformed gradient flow, which allows \mathbf{x} to move along an ascent direction on the subspace $\hat{\mathcal{V}}$ and a descent direction on the subspace $\hat{\mathcal{V}}^\perp$. The second equation in (14) is used to search for an orthonormal basis of $\hat{\mathcal{V}}$. Because the Hessian $\mathbb{H}(\mathbf{x})$ is self-adjoint, we can simply take \mathbf{v}_i as a unit eigenvector corresponding to the i th smallest eigenvalue of $\mathbb{H}(\mathbf{x})$, which can be obtained from a constrained optimization problem,

$$\min_{\mathbf{v}_i \in \mathbb{R}^n} \langle \mathbb{H}(\mathbf{x}) \mathbf{v}_i, \mathbf{v}_i \rangle, \quad \text{s.t.} \quad \langle \mathbf{v}_j, \mathbf{v}_i \rangle = \delta_{ij}, \quad j = 1, 2, \dots, i. \quad (16)$$

Then we minimize the k Rayleigh quotients (16) simultaneously by solving the second equation in (14). To avoid direction-based calculation of Hessian, we use central difference schemes for directional derivatives to approximate Hessians by k dimers centered at \mathbf{x} . The i th dimer has a direction of \mathbf{v}_i with a small dimer length $2l$ and $\mathbb{H}(\mathbf{x}) \mathbf{v}_i$ is approximated by

$$\mathbb{H}(\mathbf{x}) \mathbf{v}_i \approx \frac{\nabla E(\mathbf{x} + l \mathbf{v}_i) - \nabla E(\mathbf{x} - l \mathbf{v}_i)}{2l}. \quad (17)$$

B. Algorithm for constructing the solution landscape

The solution landscape is a pathway map consisting of all stationary points and their connections. Following the HiOSD dynamics, we construct the solution landscape by means of two algorithms: a downward search that enables us to search for all connected lower-index saddles from an index- m saddle; an upward search with a selected direction to find the higher-index saddles, which drives the entire search to navigate up and down on the energy landscape [39].

Downward search algorithm: Given an index- m saddle point $\hat{\mathbf{x}}$ and m unit eigenvectors $\hat{\mathbf{v}}_1, \dots, \hat{\mathbf{v}}_m$ corresponding to the m negative eigenvalues $\hat{\lambda}_1 \leq \dots \leq \hat{\lambda}_m$ of the Hessian $\mathbb{H}(\hat{\mathbf{x}})$ respectively, we search for a lower index- k ($k < m$) saddle point using HiOSD dynamics (14). For the initial condition, we choose $\mathbf{x}(0) = \hat{\mathbf{x}} \pm \varepsilon \mathbf{u}$ for \mathbf{x} , where we perturb the high-index saddle $\hat{\mathbf{x}}$ along the direction \mathbf{u} with a small ε to push the system away from the index- m saddle $\hat{\mathbf{x}}$. The direction \mathbf{u} is a linear combination of $(m - k)$ vectors in the set of unstable directions $\{\hat{\mathbf{v}}_{k+1}, \dots, \hat{\mathbf{v}}_m\}$, whose negative eigenvalues have the smallest magnitudes. The other k eigenvectors $\hat{\mathbf{v}}_1, \dots, \hat{\mathbf{v}}_k$ are the initial unstable directions $\mathbf{v}_i(0)$. A typical choice of initial conditions in a downward search is $(\hat{\mathbf{x}} \pm \varepsilon \hat{\mathbf{v}}_{k+1}, \hat{\mathbf{v}}_1, \dots, \hat{\mathbf{v}}_k)$. Normally, a pair of index- k saddles can be found, corresponding to the \pm sign in the initial guess. If the dynamics does not converge, a new initial condition is needed or another Morse index k is attempted.

Upward search algorithm: We can also search for a higher index- k saddle from an index- m saddle $\hat{\mathbf{x}}$ ($m < k$) by using the HiOSD dynamics. The index- m saddle is $\hat{\mathbf{x}}$ with eigenvectors $\hat{\mathbf{v}}_1, \dots, \hat{\mathbf{v}}_m$ corresponding to m negative eigenvalues. To search for a higher-index saddle, $(k - m)$ other unit eigenvectors $\hat{\mathbf{v}}_{m+1}, \dots, \hat{\mathbf{v}}_k$ corresponding to the smallest $k - m$ positive eigenvalues of the Hessian $\mathbb{H}(\hat{\mathbf{x}})$ are required. The initial state $\mathbf{x}(0)$ is set as $\hat{\mathbf{x}} \pm \varepsilon \mathbf{u}$ where \mathbf{u} is a linear combination of $\{\hat{\mathbf{v}}_{m+1}, \dots, \hat{\mathbf{v}}_k\}$, and a typical initial condition for k -HiOSD in an upward search is $(\hat{\mathbf{x}} \pm \varepsilon \hat{\mathbf{v}}_k, \hat{\mathbf{v}}_1, \dots, \hat{\mathbf{v}}_k)$.

Each downward and upward search represents a pseudodynamics between a pair of saddle points, which presents valuable insights into transition pathways between stable and unstable solutions and the corresponding energy barriers. By repeating the downward search or upward search, we are able to systematically find saddle points of various indices

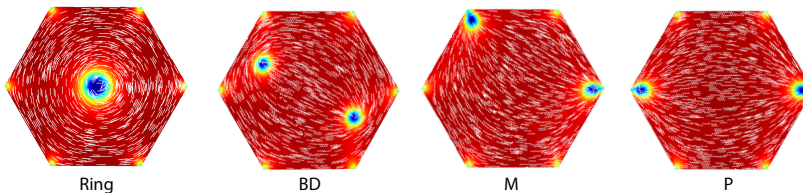


FIG. 2: Four typical solutions: Ring, BD, M, and P at $\lambda^2 = 600$.

and uncover the connectivity of the complex solution landscape. In [31], the authors identify stable reduced equilibria in different regimes and use arc continuation methods to trace the corresponding solution branches. This method misses several solution branches, particularly disconnected branches and saddle point solutions. In the next sections, we use the HiOSD method to study the solution landscape for different values of λ^2 , and as such, discover new stable solutions, saddle point solutions, e.g. TD and H solutions with multiple interior defects.

C. Spatial discretization on a hexagonal domain

To maintain the symmetric properties of the hexagonal domain, we apply finite difference schemes over triangulation to approximate the spatial derivatives in analogy with the conventional discretization of a square domain [40]. The hexagonal domain is divided into regular triangles with the edge length h , and the variable of interest ϕ is measured at the vertices. The 2D Laplacian operator is

$$\Delta = \frac{\partial^2}{\partial x^2} + \frac{\partial^2}{\partial y^2} = \frac{2}{3} \left(\frac{\partial^2}{\partial \mathbf{r}_1^2} + \frac{\partial^2}{\partial \mathbf{r}_2^2} + \frac{\partial^2}{\partial \mathbf{r}_3^2} \right), \quad (18)$$

where $\mathbf{r}_1 = (1, 0)$, $\mathbf{r}_2 = (\frac{1}{2}, \frac{\sqrt{3}}{2})$, $\mathbf{r}_3 = (-\frac{1}{2}, \frac{\sqrt{3}}{2})$, and the Laplacian can be approximated by

$$\Delta\phi(\mathbf{x}_0) \approx \frac{1}{h^2} \left(\frac{2}{3} \sum_{i=1}^3 (\phi(\mathbf{x}_0 + h\mathbf{r}_i) + \phi(\mathbf{x}_0 - h\mathbf{r}_i)) - 4\phi(\mathbf{x}_0) \right). \quad (19)$$

The elastic potential $|\nabla\phi|^2$ in (9) can also be approximated by

$$|\nabla\phi(\mathbf{x}_0)|^2 \approx \frac{1}{3h^2} \sum_{i=1}^3 ((\phi(\mathbf{x}_0 + h\mathbf{r}_i) - \phi(\mathbf{x}_0))^2 + (\phi(\mathbf{x}_0 - h\mathbf{r}_i) - \phi(\mathbf{x}_0))^2). \quad (20)$$

IV. RESULTS

A. Typical solutions on the regular hexagon

We plot some typical solutions of the reduced LdG model on a 2D hexagon in Figure 2, all of which were reported in [31]. For small enough λ , we get the Ring solution with a +1 point defect at the centre, with a high degree of symmetry. The Ring solution exists for all λ and is globally stable in the reduced framework, in the $\lambda \rightarrow 0$ limit [31]. The boundary distortion (BD) solution has two opposite +1/2 point defects near a pair of opposite edges, and this branch bifurcates from the Ring solution when the Ring solution loses stability as λ increases. There is an analogous bifurcation in a disc when the planar radial solution with a central +1 point defect bifurcates into planar polar solutions with two +1/2 point defects located along a diameter [41]. The M solutions have two point defects at vertices separated by one vertex. The P solutions are featured by a pair of diagonally opposite point defects and both the P and M solutions are stable for large enough λ . There are no interior defects in the M and P solutions. The stable Ortho (O) solutions, with two adjacent point defects at adjacent vertices, only exist for very large values of λ [31], and they will not be studied in this paper.

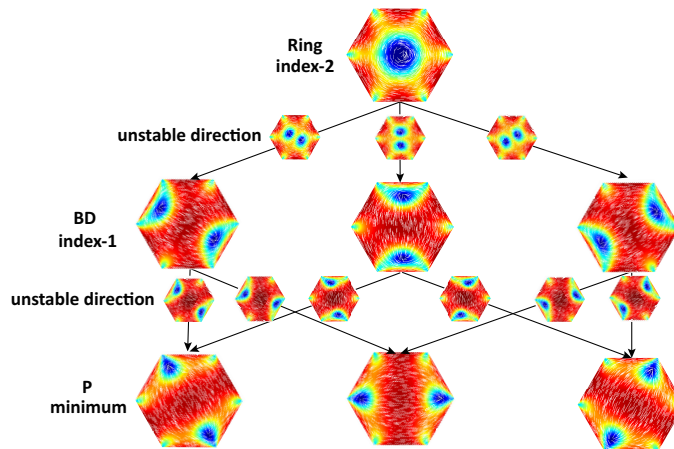


FIG. 3: Solution landscape at $\lambda^2 = 70$. Index-2 Ring is the parent state and connects to three index-1 BD solutions along its unstable directions. Each BD solution connects to two P minima along BD’s single unstable direction. The color code is related to $|\mathbf{P}|^2$ and the blue regions are defects. The white lines correspond to the planar nematic director without an arrow, since $\mathbf{n} \equiv -\mathbf{n}$ for nematics.

B. Solution landscape at $\lambda^2 = 70$

When λ^2 is sufficiently small, the Ring solution is the unique stable solution [31]. We perform an increasing λ sweep for the Ring branch using Newton’s method, the eigenvalues of the Ring solution monotonically decrease and we observe a pitchfork bifurcation at approximately $\lambda^2 \approx 10$, when we observe a transition from the unique stable Ring solution to multiple solutions [42]. For $\lambda^2 \approx 10$, the Ring solution transitions from zero index to a saddle point solution with index 2 (with two equal negative eigenvalues), and we additionally have index-1 BD solutions and index-0 P solutions. In general, we track bifurcations by tracking the indices of solutions; a change in the index is a signature of a bifurcation and a possible change of stability properties. The solution landscape for $\lambda^2 = 70$ is illustrated in Figure 3, showing the relationships between Ring, BD, and P solutions. Ring is the highest-index saddle as a parent state. Following each unstable eigendirection of the Ring solution shown in Figure 3, the center +1 point defect splits into two defects that relax around a pair of opposite edges, i.e., the BD solutions. The two BD defects move from opposite edges to opposite vertices, following the unstable eigenvector of the BD solution and converging to the corresponding P solution.

C. Solution landscape at $\lambda^2 = 120$

We obtain new saddle points in Figure 4 for $\lambda^2 = 120$. The index-3 T135 replaces the index-2 Ring as a new parent state with two degenerate negative eigenvalues and one negative eigenvalue close to zero. The new index-2 T solution has two degenerate negative eigenvalues and we deduce that these two saddle point solutions emerge from a saddle-node bifurcation, i.e., they appear suddenly without connecting with other branches in the bifurcation diagram.

Both T and T135 solutions have a central $-1/2$ point defect and three defects around alternate corners, with triangular symmetry. We can distinguish between the T and T135 solutions by zooming into the vertices (*bend-like vertex* or *splay-like vertex* in Figure 4(b)). For $\lambda^2 = 600$, we zoom into the w_1 vertex to see the differences between T and T135 more clearly. In the T solution, the $+1/3$ defect (around which the director \mathbf{n} , defined in (13), rotates by 120°) is pinned to the vertex w_1 and \mathbf{n} has a splay profile around w_1 . We refer to such a vertex with a pinned defect as a *splay-like vertex*. In T135, the $+1/3$ defect is split into a $+1/2$ interior defect and a $-1/6$ defect at w_1 (around which \mathbf{n} exhibits a 60° rotation) with a high order intermediate region between the interior $+1/2$ defect and w_1 . We refer to w_1 in T135 as a *bend-like vertex*. Regarding nomenclature, we use ‘T’ for triangular symmetry and the indices 135 to label the bend-like vertices in T135. In T135, the bend-like vertices are located at w_1, w_3 and w_5 respectively. We deduce that solutions with bend-like vertices have a higher Morse index than those with splay-like vertices. The bend-like vertices have associated interior defects and we conjecture that this results in multiple unstable directions, and hence a higher Morse index. The index-2 T solution has no bend-like vertices whereas the index-3 T135 solution has 3 bend-like vertices. More examples are given for the H and TD solutions in the next subsection.

In comparison to $\lambda^2 = 70$, we also have new connections in Figure 4(a) from T135 to T, BD and Ring respectively.

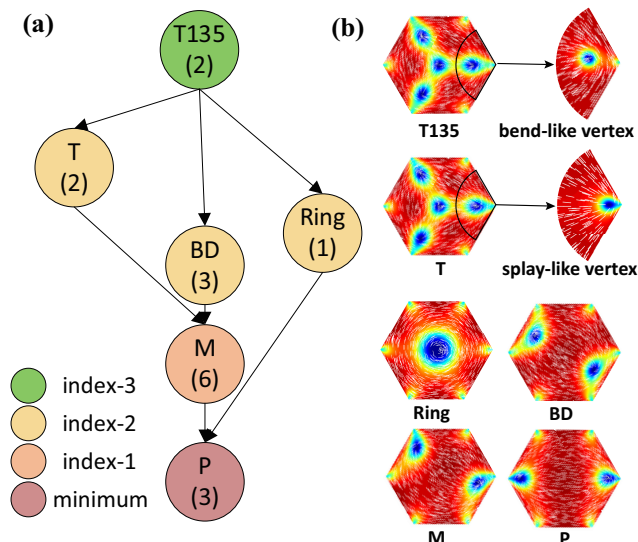


FIG. 4: (a) Solution landscape at $\lambda^2 = 120$. The colors of the nodes specify the Morse indices of saddle points. The number in the parentheses indicates the number of solutions without taking symmetry into account. The height of a node approximately corresponds to its energy (14). (b) The six configurations of solutions in (a). A zoomed-in view of w_1 for the T135 and T solutions with $\lambda^2 = 600$.

The index-1 BD saddle solution bifurcates into an index-2 BD solution and an index-1 M saddle point. We have new connections between the BD, M and P solutions and the stable P solutions are connected by the index-1 M solutions in this case.

D. Solution landscape at $\lambda^2 = 600$

The solution landscape is quite complicated at $\lambda^2 = 600$ as shown in Figure 5(a). There are three notable numerical findings in this regime: a new stable T solution with an interior $-1/2$ defect; new classes of saddle point solutions, H and TD, with high symmetry and high indices; new saddle points with asymmetric defect locations. We recover the T135 as an index-3 saddle point; the index-2 T solution bifurcates into an index-0 T and an index-1 T0; we also observe the new index-3 T130 solution and an index-2 solution, labelled as T10.

Regarding nomenclature, the 0 at the end of saddle point solutions T130, T10 and T0 indicates that the $-1/2$ defect is displaced from the centre and the other numbers label the bend-like vertices as before. We illustrate these configurations in Figure 5(a-b), and the number in parentheses is simply the number of such configurations related to each other by symmetry. The T135 and T solutions have three axes of reflection symmetry from the origin to w_1 , w_3 and w_5 respectively; T130 is symmetric with respect to reflections about the line connecting the origin to w_2 and T0 is symmetric with respect to reflections about the line connecting the origin to the vertex w_3 . The T10 saddle point has no axis of symmetry and there are 12 distinct T10 solutions, which are related to each other by symmetry considerations.

The stable index-0 T solution is our first stable solution with an interior $-1/2$ defect at the centre of the hexagon, for $\lambda^2 > 250$. The competing stable states, P and M, have defects pinned to vertices [31, 43], and these vertex defects are a natural consequence of the tangent boundary conditions and topological considerations (the total topological degree of the boundary condition is zero). We speculate that there may be other stable solutions with interior point defects, particularly on polygons with a greater number of sides, since the disc has stable planar polar solutions with two interior $+1/2$ defects. We also remark that the T solution on a hexagon for large λ is strongly reminiscent of the Ring solution on a regular triangle (Figure 5(c)), as reported in [31], which suggests that we can build new solutions by tessellating solutions on simpler building block-type polygons, such as the triangle and the square.

In the next paragraphs, we discuss saddle point solutions in the H class (Figure 6) and TD class (Figure 7) that emerge from saddle-node bifurcations and pitchfork bifurcations, with high Morse indices and multiple interior defects.

Solution landscape of the H class: We numerically find a new class of saddle point solutions, labelled as H-class solutions, which have Morse indices ranging from 8 to 14. We plot the connectivity of these solutions in Figure 6(a), and the corresponding configurations and their defect profiles in Figure 6(b).

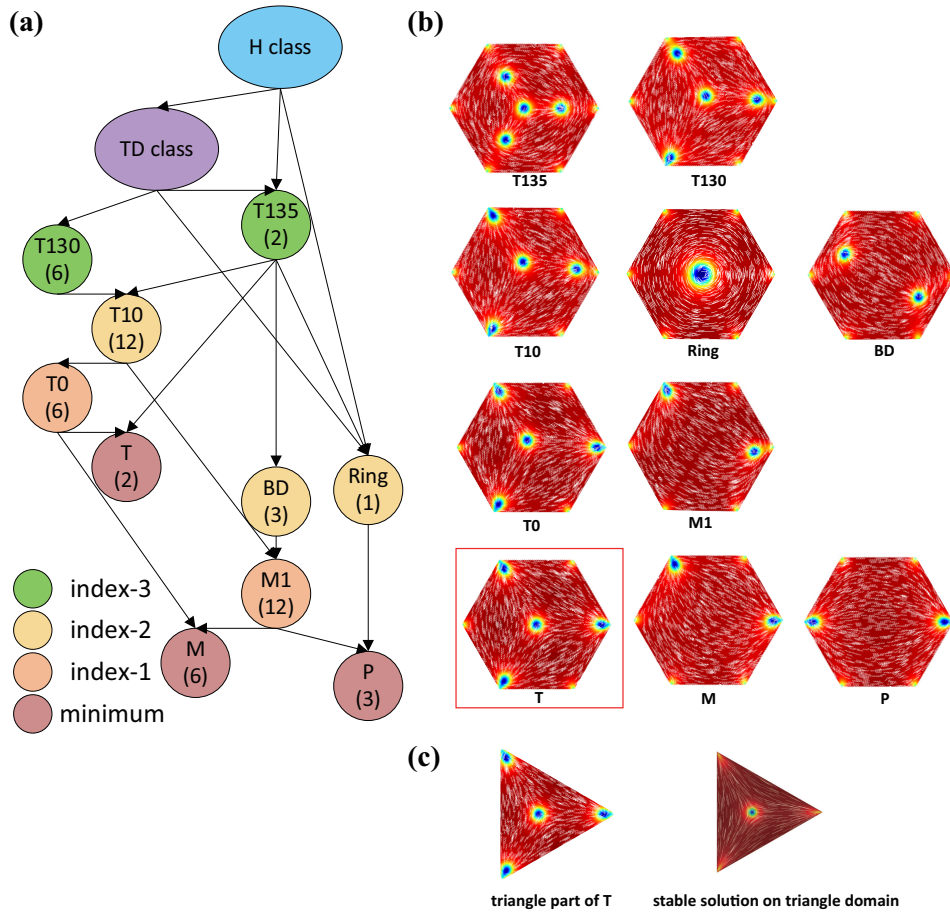


FIG. 5: (a) Solution landscape at $\lambda^2 = 600$. (b) The configurations corresponding to (a). (c) The triangle part of T solution on a hexagonal domain Ω and stable Ring solution on a triangle domain with $\lambda^2 = 450$.

The parent state is the index-14 H^* saddle point solution connecting to the lowest index-8 saddle point solution, labelled as H. Both of these states belong to the symmetry group $G_6 := \{S \in O(2) : S\Omega \in \Omega\}$ (same as the Ring solution). Regarding nomenclature, we follow the same convention as before, i.e., H135 is an H-class saddle point with bend vertices at w_1, w_3, w_5 respectively. The subscript $*$ labels the splay-like vertices (complement of bend-like vertices) so that H^* has no splay-like vertices whereas H has 6 splay-like vertices. Other examples include the index-13 $H1^*$ with one splay-like vertex w_1 and the index-9 H1 solution has one bend-like vertex w_1 ; the index-12 $H12^*$ has two splay-like vertices w_1 and w_2 and the index-10 H12 solution has two bend-like vertices at w_1 and w_2 ; the index-11 H123 solution has three bend-like vertices pinned at w_1, w_2 and w_3 respectively.

The H-class saddle points look similar at first glance and we illustrate the subtle differences by plotting $|\mathbf{P} - \mathbf{P}^H|$, where \mathbf{P} is a solution of Eq. 10 in H-class and \mathbf{P}^H is the index-8 H solution. The differences concentrate on the vertices with conspicuous red or white points in the dark blue background (Figure 6(b)). These conspicuous points are localised near or at the bend-like vertices. Numerically, we find that an index- m solution in the H class has $(m - 8)$ bend-like vertices, e.g. the index-8 H solution has no bend-like vertices whereas the index-14 H^* solution has 6 bend-like vertices.

We follow the HiOSD dynamics in Figure 6(c-d). In Figure 6(c), the unstable direction corresponding to the largest negative (closest to zero) eigenvalue of the H saddle point drives the corresponding director, \mathbf{n} in (13), to rotate clockwise or anticlockwise. Each $-1/2$ interior point defect merges with an adjacent splay-like vertex defect and disappears to give a defect-free profile around the vertex. The spiral transient state finally converges to the Ring solution. In Figure 6(d), the unstable direction corresponding to the fifth largest negative eigenvalue of index-8 H saddle point, drives three alternate $-1/2$ defects in small triangles and $+1$ defect in the center of the hexagon to combine and annihilate, yielding a $-1/2$ defect. The remaining alternate $-1/2$ defects are pushed to the edges, when the splay-like vertices disintegrate into bend-like vertices and from topological considerations, we are left with one central $-1/2$ defect and three symmetrically placed interior $+1/2$ defects. The final state is the T135 solution.

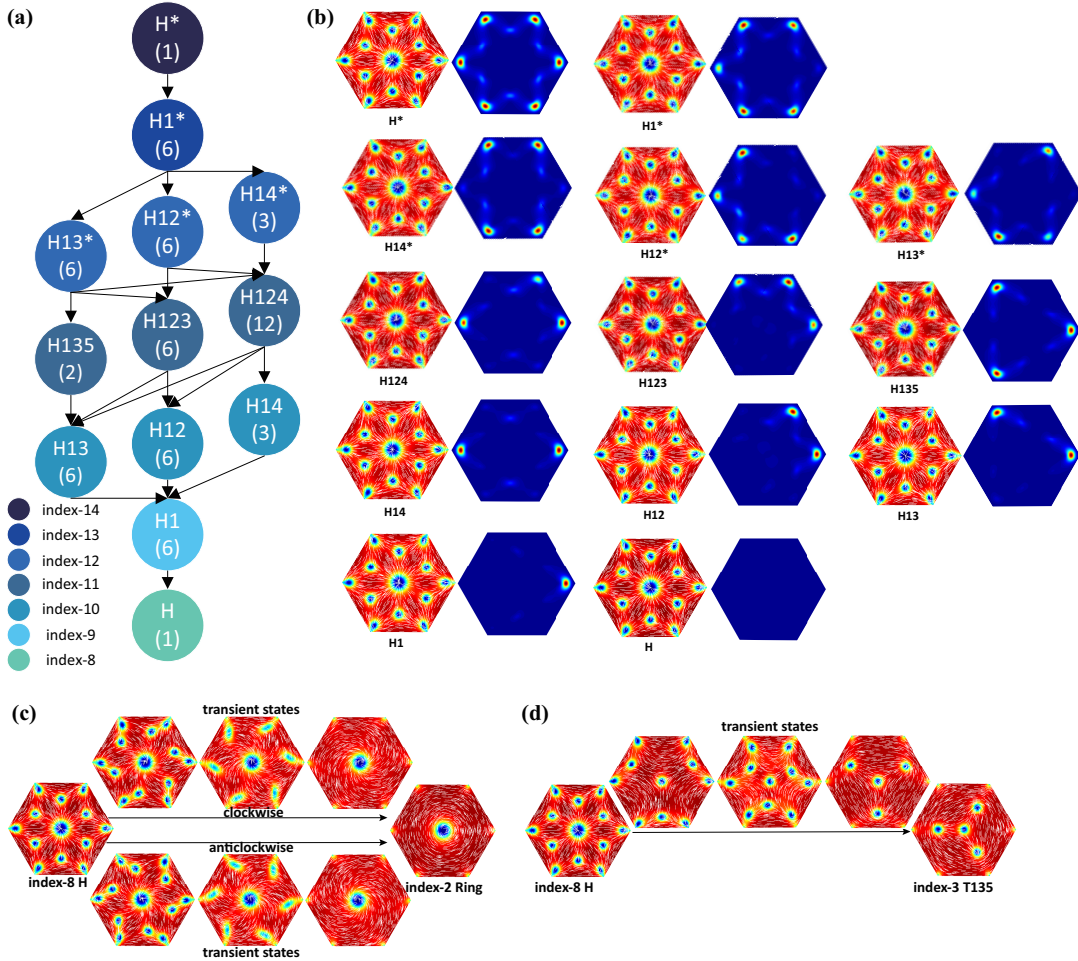


FIG. 6: (a) Solution landscape of the H class. (b) The corresponding configurations and plots of $|\mathbf{P} - \mathbf{P}^H|$, where \mathbf{P} is any solution in the H class, and \mathbf{P}^H is the index-8 H solution. (c) From index-8 H solution to index-2 Ring solution following the HiOSD dynamics (14). (d) From index-8 H solution to index-3 T135 solution following the HiOSD dynamics (14).

Solution landscape of the TD class: We use TD as an abbreviation for “triangle double” since TD solutions appear to be a superposition of two Ring solutions on a regular triangle, with two interior $-1/2$ point defects and an interior $+1/2$ point defect. The lowest-index saddle point solution in this class is the index-3 TD solution with no bend-like vertices. In general, a TD-type saddle point with m bend-like vertices is index- $(m+3)$, so that the highest-index saddle point is TD* with 3 bend-like vertices (the subscript * has no vertex label attached to it which implies that there are no splay-like vertices). All saddle points in this class have three defective vertices, either bend-like or splay-like, as suggested by our numerical results and we illustrate the connectivity of this class in Figure 7(a). The TD class can also be connected to the T130, Ring and T135 saddle points as displayed in Figure 5(a).

E. Transition pathways between stable states

We illustrate a comprehensive network of transition pathways between stable states including two T, six M and three P solutions at $\lambda^2 = 600$ in Figure 8. For clarity, we add subscripts to label the defect locations, since the hexagon is fixed and we need to cross energy barriers to switch between rotationally equivalent solutions (e.g. two different P or M solutions). In Figure 8, the T solution with defects pinned at w_2, w_4, w_6 is labelled as T_{left} and the T solution with defects pinned at w_1, w_3, w_5 is labelled as T_{right} . The subscripts in $T0_i$ simply identify the vertex closest to the displaced interior $-1/2$ defect. We use the label M1 to identify a class of index-1 saddle points, configurationally close to the M solutions, with one splay-like vertex and one bend-like vertex. We use two subscripts, i.e., $M1_{a,b}$ to identify the location of the bend-like and splay-like vertices respectively. In contrast, the stable M and P solutions have two

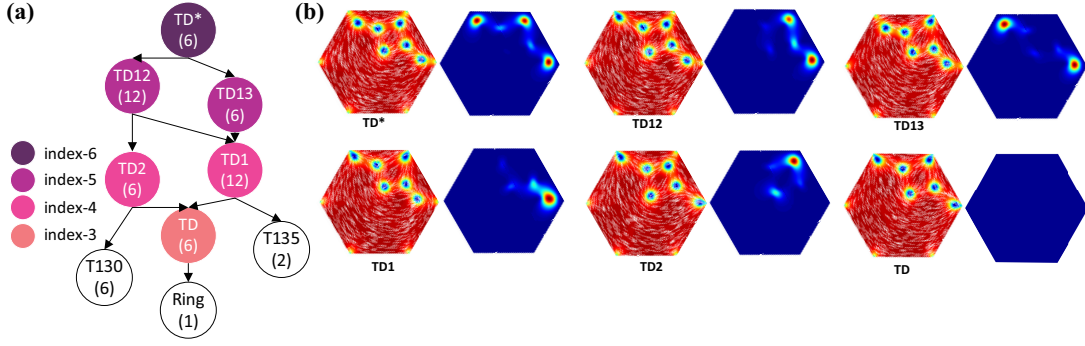


FIG. 7: (a) Solution landscape of the TD class. (b) The corresponding configurations of the TD class and plots of $|\mathbf{P} - \mathbf{P}^{TD}|$, where \mathbf{P} is any solution in the TD class, and \mathbf{P}^{TD} is the index-3 TD solution.

splay-like vertices and we use subscripts, e.g. $M_{a,b}$, to locate the splay-like vertices.

Firstly, we remark that some stable and configurationally-close solutions are connected by a single transition state (index-1 saddle point) in Figure 8. For example, the transition state between T_{left} and M_{26} is $T0_4$. The $-1/2$ center point defect in T_{left} moves towards the vertex w_4 and merges with the defect near w_4 as the configuration converges to M . The transition state between M_{26} and P_{25} is $M1_{62}$. The defect at w_6 moves towards w_5 along the edge C_5 between w_5 and w_6 , and settles at w_5 yielding the stable P_{25} state.

Secondly, two different M or P solutions cannot be connected by means of a single transition state, i.e., the transition pathway is typically composed of at least two transition pathways with an intermediate P or M state. From a practical perspective, this means that there is a high probability for the system to be trapped into the intermediate stable M or P state. For instance, one transition pathway between P_{25} and P_{36} is $P_{25} \rightarrow M1_{35} \rightarrow M_{35} \rightarrow M1_{53} \rightarrow P_{36}$. The defect at w_2 moves towards w_3 , yielding the stable M_{35} and then the defect at w_5 moves towards w_6 , yielding the stable P_{36} . Similarly, one transition pathway between M_{26} and M_{35} is $M_{26} \rightarrow M1_{26} \rightarrow P_{36} \rightarrow M1_{53} \rightarrow M_{35}$, with an intermediate stable P_{36} state. The transient dynamics involves the migration of the defect at w_2 towards w_3 , which converges to P_{36} , followed by the motion of the defect at w_6 towards the vertex w_5 to yield the final stable state M_{35} .

The most complicated transition pathway appears to be the pathway between the two T solutions: T_{left} and T_{right} . Although T_{left} and T_{right} are two symmetric solutions related by a 60° rotation, the switching process between T_{left} and T_{right} cannot be achieved by a simple rotation because the hexagonal domain is fixed. In fact, one numerically computed transition pathway between T_{left} and T_{right} is $T_{\text{left}} \rightarrow T0_4 \rightarrow M_{26} \rightarrow M1_{62} \rightarrow P_{25} \rightarrow M1_{15} \rightarrow M_{15} \rightarrow T0_3 \rightarrow T_{\text{right}}$, where $T0_4$, $M1_{62}$, $M1_{15}$ and $T0_3$ are transition states (index-1 saddle points). This shows that a transition between two energetically-close but configurationally-far T solutions may have to overcome four energy barriers and could be easily trapped by the stable M or P solutions.

In Figure 8, each transition state can connect two stable minima by following its single unstable direction. This necessarily suggests that transition states cannot connect configurationally-far stable solutions, and hence multiple transition states are needed to connect configurationally-far stable states. This is computationally expensive and as suggested before, is not a reliable way of achieving switching because of the intermediate stable states. An alternative approach is to use higher-index saddle points with multiple unstable directions, to connect configurationally-far stable solutions. The multiple unstable directions give us greater control on the dynamical pathways and offer diverse possibilities, all of which give greater insights into the design and control of solution landscapes.

Figure 9 shows how the different P, M, and T solutions are connected by high-index saddles. For instance, the index-1 $M1$ solution connects the M and P solutions and the index-1 $T0$ solution connects the stable M and T solutions. However, two M solutions or two P solutions can be connected by the index-2 BD solution, e.g. $M_{26} \leftarrow M1_{62} \leftarrow BD_{25} \rightarrow M1_{53} \rightarrow M_{35}$ and $P_{25} \leftarrow M1_{62} \leftarrow BD_{25} \rightarrow M1_{53} \rightarrow P_{36}$. The benefit of this pathway mediated by a high-index saddle point as opposed to a pathway with an intermediate stable state is that the system will not be trapped by the transient local minima along this pathway. Similarly, the M (or P) solutions and T solutions are connected by the index-2 $T10$ solution as follows: $T_{\text{left}} \leftarrow T0_4 \leftarrow T10_{42} \rightarrow M1_{26} \rightarrow P_{36}$ or M_{26} . T_{left} and T_{right} solutions are configurationally far away from each other and are thus connected by an index-8 H solution: $T_{\text{left}} \leftarrow T135_{\text{left}} \leftarrow H \rightarrow T135_{\text{right}} \rightarrow T_{\text{right}}$.

Figure 9 shows that the index-8 H solution is the stationary point in the intersection of the smallest closures of two T, three P and six M solutions on the energy landscape. The H solution is connected to every stable solution and we can thus construct dynamical pathways from the H solution to every individual stable solution. Our numerical results highlight the differences between transition pathways mediated by index-1 saddle points and pathways mediated by

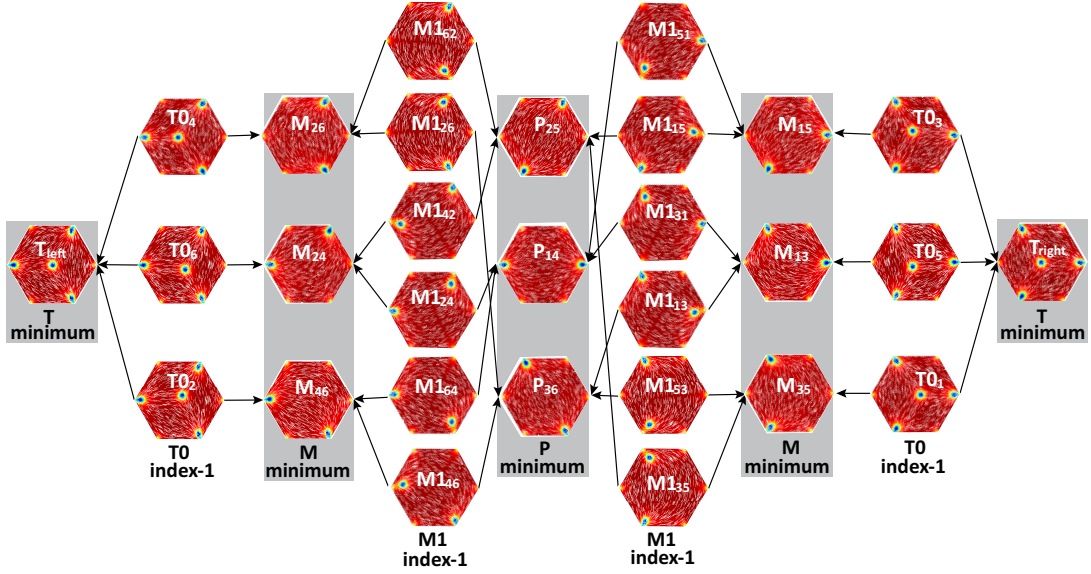


FIG. 8: The transition pathways between stable states including two T, six M and three P solutions at $\lambda^2 = 600$.

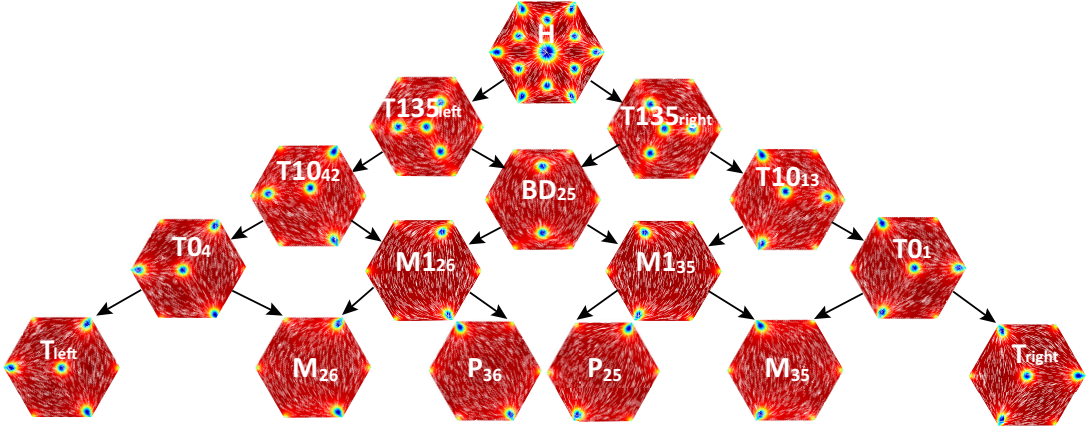


FIG. 9: Solution landscape starting from the H solution. All local minima such as T_{left} , P_{36} , M_{26} , M_{35} , P_{25} , and T_{right} are connected by the index-8 H solution.

high-index saddle points. We deduce that index-1 saddle points are efficient for connecting configurationally-close stable solutions. For configurationally-far stable states, they are generally connected by multiple transition states and intermediate stable states, or in another way, connected by a high-index saddle point.

V. COMPARISON WITH THE SOLUTION LANDSCAPE ON A SQUARE

The reduced LdG solution landscape on a square domain with tangent boundary conditions has been studied in [25] and it is known that the WORS is the unique stable LdG equilibrium for small domain sizes, exists as a stationary point for all domain sizes, and is unstable for large domain sizes [26, 27]. The WORS is special in the sense that it is characterized by two isotropic defect lines along the square diagonals. In Figure 10 (a), the Morse index of the WORS increases with the domain size and the WORS is always the parent state in the solution landscapes on a square domain. Intuitively, this is because the length of the diagonal defect lines increases as the domain size increases, and thus the WORS has an increasing number of unstable directions and an increasing Morse index with the increasing square edge length. The Ring solution that is the analogue of the WORS on a hexagon is index-0 for λ small enough and becomes an index-2 saddle point solution for larger λ , i.e., the Morse index does not increase with λ . The parent

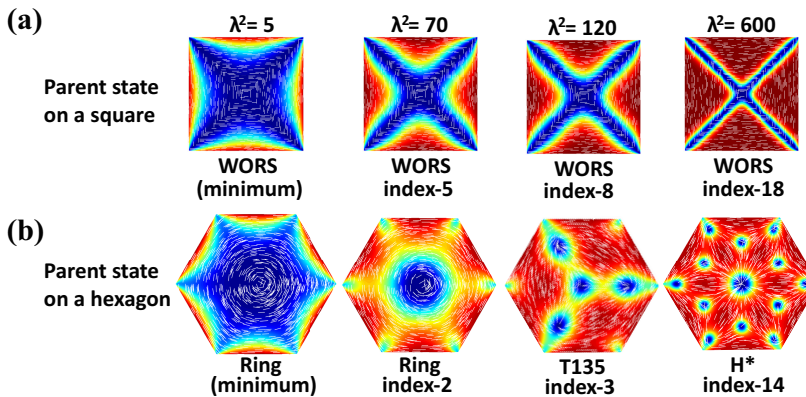


FIG. 10: Comparison of the parent states of the solution landscapes on the square (a) and the hexagon (b). The domain size $\lambda^2 = 5, 70, 120$, and 600 , respectively.

state with the highest index in the solution landscapes on a hexagon changes from the Ring solution to index-3 T135 and index-14 H^* when $\lambda^2 = 70, 120, 600$ (see Figure 10 (b)), where T135 and H^* solutions emerge through saddle-node bifurcations. In the system confined on a hexagon, we have saddle-node bifurcations, stable solutions with interior point defects, and novel T, TD- or H-class states which cannot be found for any numerically tested value of the square domain size.

Although the solution landscapes between a square domain and a hexagonal domain are quite different, there are some analogies. The WORS and the Ring solution are unique stable solutions when λ^2 , the domain size is small enough on a square and hexagon, respectively. The BD on a square or hexagon is the first unstable solution which bifurcates from the parent state, the WORS or the Ring solution respectively. The D and R solutions are stable solutions on a square [43] analogous to P and M solutions on a hexagon when λ^2 is large enough [31]. In the solution landscape on a square, $\text{WORS} \rightarrow \text{BD} \rightarrow \text{D}$ is analogous to $\text{Ring} \rightarrow \text{BD} \rightarrow \text{P}$ on a hexagon at $\lambda^2 = 70$ in Figure 3. We believe that the hexagon is a more generic example of a regular polygon with an even number of sides than a square and hence, we expect the qualitative aspects of our numerical study to extend to other regular polygons with an even number of sides.

VI. CONCLUSION

We investigate the solution landscape of a reduced LdG model on a regular 2D hexagon with tangent boundary conditions, as a prototype problem concerning nematic equilibria on regular 2D domains. We study reduced LdG energy minima in [31], and report the Ring solution for nano-scale hexagons, and the P and M stable states for larger micron-scale hexagons, including a bifurcation diagram for the solution branches as a function of λ^2 , i.e., we trace the continuation of these solution branches as a function of the hexagon size. We go much further in this manuscript in the sense that we focus on the solution landscape including both minima and saddle points, and their relationships. We first present illuminating numerical results on how the Morse index of solutions changes with λ , i.e., the Ring solution with a stable central $+1$ defect is index-0 for small λ and is index-2 for large λ . Similarly, the BD solution branch changes from index-1 to index-2 as λ increases. This is an interesting numerical example on how a given solution becomes more unstable as a function of the geometry. We observe new solution branches, e.g. TD- and H-class saddle points through saddle-node bifurcations, and quite importantly, we report two new stable T solutions with a central $-1/2$ defect, surrounded by three splay-like vertices. In fact, the T solution gains stability as λ increases, with a transition from index-2 to index-0 as λ increases, and is reminiscent of the Ring solution for a regular triangle superimposed on a hexagonal domain [31]. This raises the pertinent question—can we construct reduced solutions on complex geometries by using reduced solutions on simpler geometries as a building block? We illustrate the solution landscapes at three representative values of λ^2 and strongly speculate that there are more stable solutions, symmetric and asymmetric saddle point solutions, tessellated solutions as λ increases. Further, since the Dirichlet boundary condition is either topologically trivial or has a unit degree, we could build a further hierarchy of exotic reduced solutions by exploiting the topological degree of the tangent boundary condition.

A further innovative aspect of our study are insightful numerical results on dynamical pathways. We present several informative examples of transition pathways with a single transition state, multiple transition states and pathways

mediated by higher-index saddle points. We believe that pathways mediated by high-index saddle points give greater possibilities for transition pathways, without the risk of being trapped into metastable states, and we can control the dynamical pathways by manipulating different unstable directions. The selective mechanism for dynamical pathways, in other words, how a system chooses between multiple dynamical pathways connecting a pair of equilibria, remains an open problem of practical significance for liquid crystal devices.

We also remark that our results, though restricted to a 2D setting, will survive in a 3D setting too, for example on a well with a 2D hexagon as cross-section [33]. In fact, the Ring solution will survive as a translationally invariant solution on a 3D well, for arbitrary well heights, and will be globally stable for λ small enough, independently of the well height. It is not clear if the Morse index of the saddle points will increase in a 3D setting and we expect this to be strongly dependent on the boundary conditions in a 3D setting.

The results in this paper pose several challenging analytic and numerical questions. Can we obtain bounds for the Morse index as a function of λ ? Is there an upper bound independent of λ , which would also impose restrictions on the complexity of the solution landscape with increasing λ ? A reduced LdG tensor only has two degrees of freedom whereas the full LdG tensor in 3D has five degrees of freedom. We speculate that the T solution on a hexagon may not be stable in a fully 3D framework. Other natural generalizations include the effects of the asymmetry in geometry, or the effects of elastic anisotropy and preliminary work shows that elastic anisotropy perturbs the symmetry of the problem, so that we may lose the Ring solution and the WORS with elastic anisotropy. Notably, we lose the structure of the Laplacian in the Euler-Lagrange equations that makes the problem analytically and computationally complex, with elastic anisotropy. We defer these investigations of the dimensionality, geometrical features and material anisotropy to future work.

Acknowledgment This work was supported by National Natural Science Foundation of China No. 11861130351, 21790340, 11421101, and the Royal Society Newton Advanced Fellowship awarded to Lei Zhang and Apala Majumdar.

-
- [1] P. G. de Gennes and J. Prost. *The physics of liquid crystals*, volume 83. Oxford university press, 1995.
- [2] L. Zhang, L. Q. Chen, and Q. Du. Morphology of critical nuclei in solid-state phase transformations. *Physical Review Letters*, 98(26):265703, 2007.
- [3] Y. C. Han, Z. R. Xu, A. C. Shi, and L. Zhang. Pathways connecting two opposed bilayers with a fusion pore: a molecularly-informed phase field approach. *Soft Matter*, 2020.
- [4] T. Takashi and N. Yasumasa. Morphological characterization of the diblock copolymer problem with topological computation. *Japan Journal of Industrial & Applied Mathematics*, 27(2):175–190, 2010.
- [5] L. Zhang, W. Q. Ren, A. Samanta, and Q. Du. Recent developments in computational modelling of nucleation in phase transformations. *NPJ Computational Materials*, 2:16003, 2016.
- [6] O. D. Lavrentovich, P. Pasini, C. Zannoni, and S. Žumer. *Defects in liquid crystals: Computer simulations, theory and experiments*, volume 43. Springer Science & Business Media, 2012.
- [7] I. Mušević, M. Škarabot, U. Tkalec, M. Ravnik, and S. Žumer. Two-dimensional nematic colloidal crystals self-assembled by topological defects. *Science*, 313(5789):954–958, 2006.
- [8] G. Foffano, J. S. Lintuvuori, A. Tiribocchi, and D. Marenduzzo. The dynamics of colloidal intrusions in liquid crystals: A simulation perspective. *Liquid Crystals Reviews*, 2(1):1–27, 2014.
- [9] T. C. Lubensky, D. Petey, N. Currier, and H. Stark. Topological defects and interactions in nematic emulsions. *Physical Review E*, 57(1):610, 1998.
- [10] L. Onsager. The effects of shape on the interaction of colloidal particles. *Annals of the New York Academy of Sciences*, 51(1):627–659, 1949.
- [11] I. Bajc, F. Hecht, and S. Žumer. A mesh adaptivity scheme on the Landau–de Gennes functional minimization case in 3D, and its driving efficiency. *Journal of Computational Physics*, 321:981–996, 2016.
- [12] A. Majumdar and Y. W. Wang. Remarks on uniaxial solutions in the Landau–de Gennes theory. *Journal of Mathematical Analysis and Applications*, 464(1):328–353, 2018.
- [13] A. Majumdar and A. Zarnescu. Landau-de Gennes theory of nematic liquid crystals: the Oseen–Frank limit and beyond. *Archive for Rational Mechanics and Analysis*, 196(1):227–280, 2010.
- [14] D. Henao, A. Majumdar, and A. Pisante. Uniaxial versus biaxial character of nematic equilibria in three dimensions. *Calculus of Variations and Partial Differential Equations*, 56(2):55, 2017.
- [15] L. Nguyen and A. Zarnescu. Refined approximation for minimizers of a Landau-de Gennes energy functional. *Calculus of Variations and Partial Differential Equations*, 47(1-2):383–432, 2013.
- [16] L. Zhang, Q. Du, and Z. Z. Zheng. Optimization-based shrinking dimer method for finding transition states. *SIAM Journal on Scientific Computing*, 38(1):A528–A544, 2016.
- [17] H. Kusumaatmaja and A. Majumdar. Free energy pathways of a multistable liquid crystal device. *Soft matter*, 11(24):4809–4817, 2015.
- [18] Y. C. Han, Y. C. Hu, P. W. Zhang, and L. Zhang. Transition pathways between defect patterns in confined nematic liquid crystals. *Journal of Computational Physics*, 396:1–11, 2019.

- [19] J. W. Milnor, M. Spivak, and R. Wells. *Morse theory*, volume 1. Princeton university press Princeton, 1969.
- [20] Y. X. Li and J. X. Zhou. A minimax method for finding multiple critical points and its applications to semilinear PDEs. *SIAM Journal on Scientific Computing*, 23(3):840–865, 2001.
- [21] P. E. Farrell, Á. Birkisson, and S. W. Funke. Deflation techniques for finding distinct solutions of nonlinear partial differential equations. *SIAM Journal on Scientific Computing*, 37(4):A2026–A2045, 2015.
- [22] J. P. K. Doye and D. J. Wales. Saddle points and dynamics of Lennard-Jones clusters, solids, and supercooled liquids. *The Journal of Chemical Physics*, 116(9):3777–3788, 2002.
- [23] D. Mehta. Finding all the stationary points of a potential-energy landscape via numerical polynomial-homotopy-continuation method. *Physical Review E*, 84:025702, 2011.
- [24] W. R. Hao, J. D. Hauenstein, B. Hu, and A. J. Sommese. A bootstrapping approach for computing multiple solutions of differential equations. *Journal of Computational and Applied Mathematics*, 258:181–190, 2014.
- [25] J. Y. Yin, Y. W. Wang, J. Z. Y. Chen, P. W. Zhang, and L. Zhang. Construction of a pathway map on a complicated energy landscape. *Physical Review Letters*, 124:090601, 3 2020.
- [26] S. Kralj and A. Majumdar. Order reconstruction patterns in nematic liquid crystal wells. *Proceedings of the Royal Society A: Mathematical, Physical and Engineering Sciences*, 470(2169):20140276, 2014.
- [27] G. Canevari, A. Majumdar, and A. Spicer. Order reconstruction for nematics on squares and hexagons: A Landau-de Gennes study. *SIAM Journal on Applied Mathematics*, 77(1):267–293, 2017.
- [28] J. Y. Yin, L. Zhang, and P. W. Zhang. High-index optimization-based shrinking dimer method for finding high-index saddle points. *SIAM Journal on Scientific Computing*, 41(6):A3576–A3595, 2019.
- [29] D. Golovaty, J. A. Montero, and P. Sternberg. Dimension reduction for the Landau–de Gennes model on curved nematic thin films. *Journal of Nonlinear Science*, 27(6):1905–1932, 2017.
- [30] F. Bethuel, H. Brezis, F. Hélein, et al. *Ginzburg-Landau Vortices*, volume 13. Springer, 1994.
- [31] Y. C. Han, A. Majumdar, and L. Zhang. A reduced study for nematic equilibria on two-dimensional polygons. *arXiv preprint arXiv:1910.05740*, 2019.
- [32] P. J. Wojtowicz, P. Sheng, and E. B. Priestley. *Introduction to liquid crystals*. Springer, 1975.
- [33] G. Canevari, J. Harris, A. Majumdar, and Y. W. Wang. The well order reconstruction solution for three-dimensional wells, in the Landau-de Gennes theory. *International Journal of Nonlinear Mechanics*, 119:103342, 2020.
- [34] A. Brodin, A. Nych, U. Ognysta, B. Lev, V. Nazarenko, M. Škarabot, and I. Muševič. Melting of 2D liquid crystal colloidal structure. *Condensed Matter Physics*, 2010.
- [35] A. Majumdar, Y. W. Wang, B. Varsha, and K. Bisht. Tailored morphologies in 2D ferronematic wells. *Europhysics Letters*, 2019.
- [36] G. Gupta and A. D. Rey. Texture modeling in carbon–carbon composites based on mesophase precursor matrices. *Carbon*, 43(7):1400–1406, 2005.
- [37] I. Musevic and M. Skarabot. Self-assembly of nematic colloids. *Soft Matter*, 4(2):195–199, 2008.
- [38] I. Musevic, M. Skarabot, U. Tkalec, M. Ravnik, and S. Zumer. Two-dimensional nematic colloidal crystals self-assembled by topological defects. *Science*, 313(5789):954–958, 2006.
- [39] J. Y. Yin, B. Yu, and L. Zhang. Searching the solution landscape by generalized high-index saddle dynamics. *arXiv preprint arXiv:2002.10690*, 2020.
- [40] J. C. Fabero, A. Bautista, and L. Casasús. An explicit finite differences scheme over hexagonal tessellation. *Applied Mathematics Letters*, 14(5):593–598, 2001.
- [41] Y. C. Hu, Y. Qu, and P. W. Zhang. On the disclination lines of nematic liquid crystals. *Communications in Computational Physics*, 19(2):354–379, 2016.
- [42] H. Troger and A. Steindl. *Nonlinear stability and bifurcation theory: an introduction for engineers and applied scientists*. Springer Science & Business Media, 2012.
- [43] M. Robinson, C. Luo, P. E. Farrell, R. Erban, and A. Majumdar. From molecular to continuum modelling of bistable liquid crystal devices. *Liquid Crystals*, 44(14-15):2267–2284, 2017.